Supplemental Document

Optics Letters

Delay-and-sum-to-delay-standard-deviation factor: a promising adaptive beamformer: supplement

Souradip Paul, Anjali Thomas, and Mayanglambam Suheshkumar Singh*

School of Physics, Indian Institute of Science Education and Research Thiruvananthapuram, Thiruvananthapuram 695551, India
**Corresponding author: suhesh.kumar@iisertvm.ac.in*

Supplement DOI: https://doi.org/10.6084/m9.figshare.16413285

Parent Article DOI: https://doi.org/10.1364/OL.437394

SUPPLEMENTARY 1: NUMERICAL SIMULATION USING K-WAVE MATLAB PLATFORM

For validation study of the experimental results, we carried out numerical simulation studies where a linear transducer array consisting of 16 sensor elements − similar to that of the experimental studies − is adopted as acoustic sensor for boundary detection of the PA-signals. We also carried out simulation studies with linear array transducer consisting of 128 sensor elements, which is very standard and commonly used in linear array-based photoacoustic imaging (PAI) and ultrasound (US) imaging).

For numerical simulation, we employed k-Wave MATLAB toolbox which is commonly and widely used in PA-imaging as a numerical simulation tool [1–3]. Eight circular targets of radius $\sim 0.1mm$ were embedded in a homogeneous background medium (of $60mm$ (in axial direction) and $20mm$ (in lateral direction)) along the vertical z-axis with a separation of $5mm$ between two consecutive targets. For all of the targets, strength of the initial PA pressure waves was tailored to be $5Pa$ against $0Pa$ (for the background, as it is done in [4, 5]) while mass density, speed of sound, and acoustic attenuation coefficient were tailored to be similar as $1000kg/m^3$, $1500m/s$, and $0.75dB/(MHz.cm)$ respectively. The first target was placed at a distance of $18mm$ away from the transducer surface which is a linear-array sensor consisting of 16 elements with an inter-element spacing $\sim 1.2mm$, central frequency $\sim 7.5MHz$, and bandwidth $\sim 60\%$. From this array of boundary measured time-resolved PA-signals, we reconstructed the spatial distribution of PA-signal strength and thus, generate the reconstructed images. The entire 16 sensor elements are grouped into 4 sub-arrays with 4 sensor elements (given by $L = \frac{16}{4}$) in each sub-arrays (as it is done in the experimental studies). The detected signals were sampled with sampling frequency $\sim 50MHz$. Envelope detection (using Hilbert transform) followed by log compression were performed in the beamformed signals and then, normalized before displaying the reconstructed images. The simulation results are presented in Fig. 1-2 and Table 1 in the main text.

In most of the commercially available US and PA imaging systems (including Verasonic Inc., USA and Cyberdine Inc., Japan), 128 element transducers are commonly used to collect the boundary data. Moreover, there are several reported articles where studies were performed using linear array transducer of 128 sensor elements. To follow and compare with this standard linear transducer-based imaging system, we carried out simulation studies with linear transducer array of 128 elements where we replaced the linear transducer of 16 elements by that of 128 elements in the above mentioned numerical simulation procedure (for the case of 16 elements). In the case of linear transducer with 128 elements, the entire 128 sensor elements are grouped into 4 sub-arrays with 32 sensor elements (given by $L = \frac{128}{4}$) in each sub-arrays. The reconstructed PA-images − corresponding to linear US transducer consisting of 128 sensor elements − are presented in Fig. S1. From the results (shown in Fig. S1), it is clearly observable that our proposed algorithm outperforms the existing reconstruction algorithms (namely, MV and $MV + CF$).

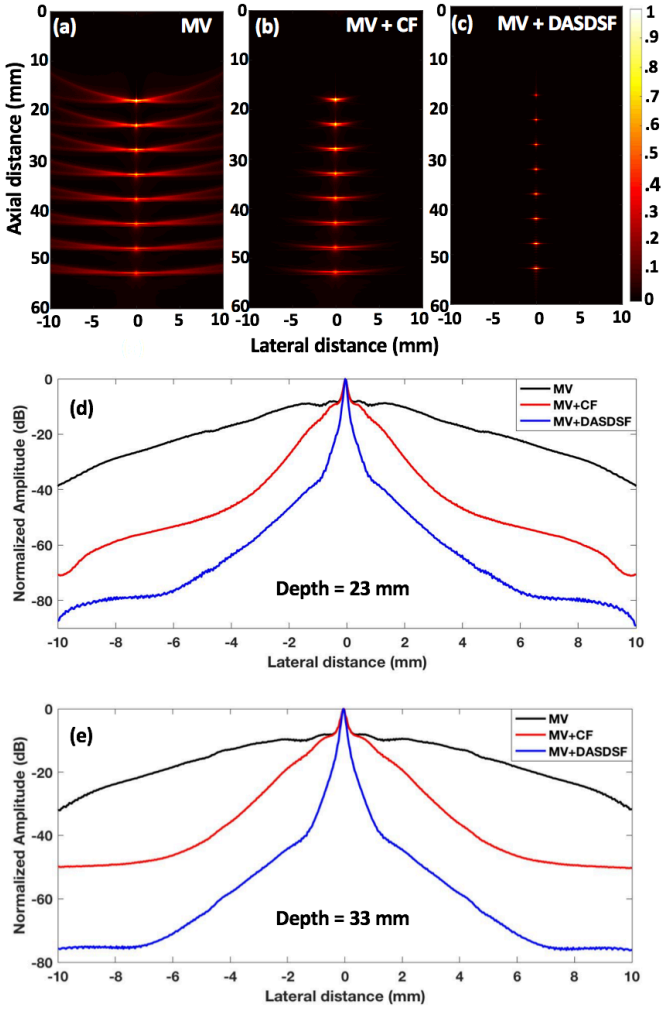

Fig. S1: Reconstructed PA-images of a numerical phantom with eight point targets − being embedded (along a vertical axis) in background − using various beamformers: MV (a), $MV + CF$ (b), and $MV + DASDSF$ (c).Variation of PA-signal strength along the lateral direction across the targets at the depths $\sim 23mm$ (d) and $\sim 33mm$ (e). We employed linear array transducer of 128 sensor elements (against 16 elements as it is shown in Fig. 1-2).

SUPPLEMENTRY 2: NUMERICAL SIMULATION STUDIES FOR VALIDATION OF SIGNAL CROSS-TALKS FROM CLOSELY SPACED TARGETS

To validate the image reconstruction performance of the proposed algorithm under high influence of side-lobes and/or cross-talks of PA-signals from closely spaced targets, we considered a numerical sample or phantom embedded with closely spaced five (5) individual circular targets (radius $\sim 0.1mm$) being arranged in a row (in lateral direction) at the depth of $\sim 25mm$ from the transducer surface. Each targets is physically separated from one another by $\sim 1.2mm$. Fig. S2(a)-(c) present the reconstructed images of the numerical phantom (consisting of five targets) obtained by using the existing algorithms (MV and $MV + CF$) and our proposed algorithm ($MV + DASDSF$). From the reconstructed images, we observed that, in the reconstructed image obtained by using MV, the individual targets are not only highly overlapped but also corrupted by side lobes at a

greater extent. When MV is combined with coherence factor (CF), side-lobes are significantly reduced and targets are detectable but feebly. In the reconstructed image obtained by our proposed ($MV + DASDSF$) technique, the five individual targets are clearly visible and well-resolved but also the side-lobes (marked blue color arrow lines in Fig. S2(a)-(b)) are significantly removed or filtered. These results demonstrate that our proposed $MV + DASDSF$ outperforms the existing algorithms in suppressing the side-lobes as well as reconstructing closely spaced point targets with higher resolution and SNR, i.e., filtering the cross-talks of interfering signals. This is because of compensation of coherency in the PA-signals while arriving at a given reconstruction point (as it is discussed in the article).

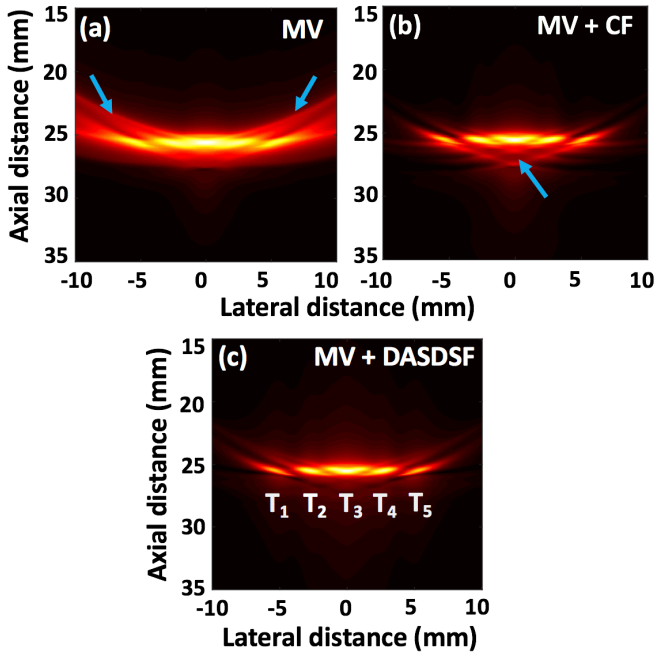

Fig. S2: Reconstructed images of the numerical phantom, consisting of five closely spaced targets in a row, which are obtained by: (a) MV, (b) $MV + CF$ and (c) $MV + DASDSF$.

SUPPLEMENTARY 3: COMPARISON OF IMAGING PERFORMANCE OF OUR PROPOSED ALGORITHM WITH THE EXISTING ALGORITHMS AT VARIOUS IMAGING DEPTHS.

In Fig. 2 and Table 1 (presented in the main text), out of the eight imaging targets (shown in Fig. 1 in the main text), the quantitative comparison of imaging performance is presented only for two representative targets. This is because of page-limit provided in this article. In this supplementary section, we present the quantitative comparison of imaging performance for all of the eight targets at different imaging depths, i.e., quantitative comparison of imaging performance of our proposed algorithm with state-of-the-art algorithms at various imaging depths. Fig. S3(a) gives plot of variation of the obtainable spatial resolution (represented by $FWHM$) with respect to imaging depth for different image reconstruction algorithms while Fig. S3(b) gives variation of SNR with respect to imaging depth. In these figures, we observe that the obtainable spatial resolution and SNR of the reconstructed images degrade in linear fashion for all of the algorithms (as it is indicated by linear curve-fittings included in the figures). From Fig. S3(a), we can conclude that our proposed algorithm gives higher spatial resolution and the obtainable image resolution does not degrade or remains almost constant with the imaging depth (unlike the other state-of-the-art algorithms which give spatial resolution being degraded with the imaging depth) as it is indicated by magnitudes of the corresponding slopes. We clearly observe (see Fig. S3(b)) that SNR of the reconstructed images with our proposed algorithm is significantly enhanced in comparison to other existing algorithms. The results demonstrate that our proposed algorithm improves imaging performance in terms of obtainable spatial resolution as well as SNR (in comparison to MV and $MV + CF$).

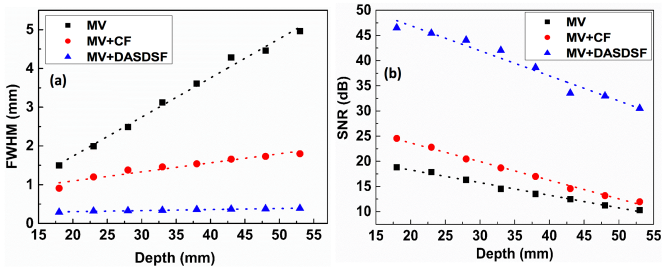

Fig.S3: Plot of variation of $FWHM$ (a) and SNR (b) with respect to imaging depth (corresponding to eight simulated point targets). Linear curve-fittings to the experimental data are depicted in the figures.

SUPPLEMENTARY 4: SCHEMATIC DIAGRAM OF THE EXPERIMENTAL SET-UP

To evaluate the imaging performance of our proposed algorithm, we conducted experiments in both tissue-mimicking Agar phantom as well as (ex-vivo) tissue (chicken breast from supermarket). For the experiments, we employed our home-built photoacoustic tomography (PAT) imaging system which is mentioned as PAI in this article. In this PAT system, we employed a tuneable pulsed OPO laser (SpitLight EVO S OPO-355, Innolas Lasers, Germany, tuneable wavelengths $\sim 415 - 670nm$, pulse width $\sim 6nm$, tuneable pulse repetition frequency (PRF)

$\sim 1-100Hz$) that generates a highly collimated optical (pulse) beam. As it is shown in the schematic diagram (S4(b)). We used an adaptable optical fiber cable (OFC) to couple the output laser beam from the laser source and thus, deliver the pulse optical beam to the imaging sample of interest. In our present experimental studies, we employed pulsed laser beam of wavelength $\sim 532nm$, pulse-width $\sim 6ns$, and PRF $\sim 100Hz$. Energy of the laser beam was kept less than FDA safety limit ($22mJ/cm^2$). For boundary detection of PA-signals, that are induced by transient optical illumination of the sample due to photoacoustic effect [6], we employed a low cost ($\sim INR\ 3,50,000$) 16 element linear array transducer-based US system (Kae16D, Surabi Biomedical Instrumentation, India) of center frequency $\sim 3MHz$, bandwidth $\sim 3MHz$ and pitch-width $1.2mm$ to pick-up the PA-signals from the targets (in reflection configuration). The transducer and the OFC are housed in a home-made holding unit and the holding unit as a whole is kept attached to motion-controlled unit that is constituted by stepper motors (Newmark NSC-G3, Newmark Systems Inc., USA). This motion-controlled system facilitates a precise control of movement of the PAT imaging system in all of three possible (xyz) directions with a step-size resolution of $80nm/step$. These 16 sensor elements in the linear transducer serve as closely spaced individual and independent (acoustic) sensors and generate an array of time-resolved PA-signal data as an output from the US system. Corresponding to an optical pulse or pulse optical beam (of pulse width $\sim 6nm$), these individual 16 sensors simultaneously acquire PA-signals. At one scanning position, the imaging system collect 2D-data corresponding to a 2D-cross-sectional plane (say, $zx-$plane where the linear sensor elements are aligned along $x-$axis while the axis of transducer is aligned along $z-$axis) of the imaging specimen. By extending the scanning along y-axis, we can obtain 3D data and thus, 3D reconstructed images. The entire PAT imaging system is synchronized and controlled by a LabVIEW-based software that is developed in our laboratory. As it is mentioned in the article, this array of time-resolved PA-signals were employed for image reconstruction. In the similar way to the numerical simulation study, the entire 16 sensor elements or set of time-resolved data are sub-grouped into 4. We adapted envelope detection (using Hilbert transform) followed by log compression in the beamformed signals.

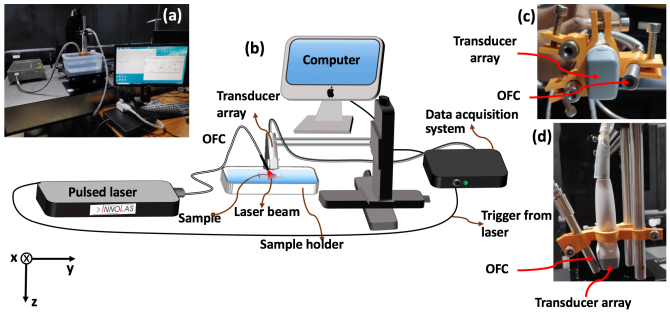

Fig. S4: Photograph of the home-built photoacoustic tomography (PAT) imaging system (a) and the corresponding schematic diagram (b). Front view (c) and side view (d) of the assembly of linear array transducer and optical fiber cable (OFC) in holding unit.

SUPPLEMENTARY 5: EXPERIMENTAL RESULTS FOR AGAR TISSUE-MIMICKING PHANTOM

We also performed experiments in tissue-mimicking Agar phantom to further evaluate the proposed method to a greater extent. The phantom consists of four black wires, two of which were placed near to each other ($\sim 2.5mm$) and at the same depth. The other two were are set $\sim 4mm$ above and $\sim 5mm$ below from the middle of the two targets. All of the wires, which are serving as the imaging targets, were embedded in background Agar phantom with concentration $\sim 1\%$. While acquiring the PA-signals, the ultrasound probe was kept perpendicularly to the four wires. From the reconstructed images (see Fig. S5), it is clearly observable that our proposed $DASDSF$ beamforming reduces sidelobes and background noises (dotted circle in Fig. S5(d)) significantly. In addition, targets are discernible (as they are indicated by blue color arrow lines in Fig. S5(d)) with better resolution and higher signal strength (SNR) in comparison to that of the conventional methods. The line-plot $-$ at depth $\sim 34mm$ showing the variation of PA-signal strength (along a line in lateral direction at the depth $\sim 34mm$) $-$ demonstrates that our proposed algorithm gives higher resolution (indicated by green color arrow lines in Fig. S5(e)), lower background noises (indicated by green color dotted circle in Fig. S5(e)), and higher signal contrast.

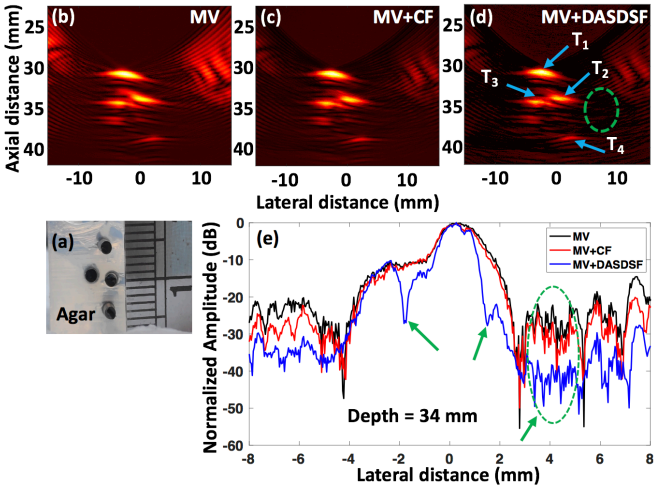

Fig. S5: Reconstructed PA-images of the agar phantom (with the four wires being embedded in backgorund Agar phantom (photography of a cross-section of the phantom is shown in (a))) using (b) MV, (c) $MV + CF$, and (d) $MV + DASDSF$. (e) Line-plot of variation of PA-signal strength along a line in lateral direction at depth $\sim 34mm$ using our proposed reconstruction technique in comparison to the conventional techniques.

SUPPLEMENTRY 6: COMPUTATION TIME TAKEN BY DIFFERENT BEAMFORMING ALGORITHMS FOR *EX-VIVO* CHICKEN SAMPLE

To compare the computing performance, the beamforming algorithms were tested on a portable laptop computer with Intel Core i5-8565 CPU at $1.80GHz$ and $8GB$ RAM to compare the computing performance. The computational reconstruction time using MV, $MV + CF$ and $MV + DASDSF$ are $35.46sec.$, $35.69sec.$, and $35.82sec.$ respectively for the *ex-vivo* imaging. It is noticed that the reconstruction time of the proposed method is close to other existing beamforming algorithms.

REFERENCES

1. B. E. Treeby and B. T. Cox, J. Biomed. Opts. **15**, 314–021 (2010).
2. S. Paul, S. Rajendran, and M. S. Singh, TENCON 2019-2019 IEEE Reg. 10 pp. 91–95 (2019).
3. M. S. Singh and P. K. Yalavarthy, "Born-ratio type data normalization improves quantitation in photoacoustic tomography," in *Medical Imaging 2014: Ultrasonic Imaging and Tomography,* , vol. 9040 (International Society for Optics and Photonics, 2014), p. 90401T.
4. M. Mozaffarzadeh, A. Mahloojifar, M. Orooji, K. Kratkiewicz, S. Adabi, and M. Nasiriavanaki, J. Biomed. Opts. **23**, 026002 (2018).
5. M. Mozaffarzadeh, Y. Yan, M. Mehrmohammadi, and B. Makkiabadi, J. Biomed. Opts. **23**, 026005 (2018).
6. M. S. Singh, S. Paul, and A. Thomas, "Fundamentals of photoacoustic imaging: A theoretical tutorial," in *LED-Based Photoacoustic Imaging,* (Springer, 2020), pp. 3–21.

FULL REFERENCES

1. B. E. Treeby and B. T. Cox, "k-wave: Matlab toolbox for the simulation and reconstruction of photoacoustic wave fields," J. Biomed. Opts. **15**, 314–021 (2010).
2. S. Paul, S. Rajendran, and M. S. Singh, "k-wave toolbox for studying elastic property in photoacoustic imaging," TENCON 2019-2019 IEEE Reg. 10 pp. 91–95 (2019).
3. M. S. Singh and P. K. Yalavarthy, "Born-ratio type data normalization improves quantitation in photoacoustic tomography," in *Medical Imaging 2014: Ultrasonic Imaging and Tomography,* vol. 9040 (International Society for Optics and Photonics, 2014), p. 90401T.
4. M. Mozaffarzadeh, A. Mahloojifar, M. Orooji, K. Kratkiewicz, S. Adabi, and M. Nasiriavanaki, "Linear-array photoacoustic imaging using minimum variance-based delay multiply and sum adaptive beamforming algorithm," J. Biomed. Opts. **23**, 026002 (2018).
5. M. Mozaffarzadeh, Y. Yan, M. Mehrmohammadi, and B. Makkiabadi, "Enhanced linear-array photoacoustic beamforming using modified coherence factor," J. Biomed. Opts. **23**, 026005 (2018).
6. M. S. Singh, S. Paul, and A. Thomas, "Fundamentals of photoacoustic imaging: A theoretical tutorial," in *LED-Based Photoacoustic Imaging,* (Springer, 2020), pp. 3–21.